Article

Synthesis and Characterization of Ce^{3+}-Doped $Ni_{0.5}Cd_{0.5}Fe_2O_4$ Nanoparticles by Sol–Gel Auto-Combustion Method

Danyal Ahmad [1,*], Nasir Mehboob [1], Abid Zaman [1,*], Nabeel Ahmed [1], Kashif Ahmed [1], Muhammad Mushtaq [2], Khaled Althubeiti [3], Asad Ali [1,4], Fozia Sultana [5] and Khalid Bashir [1]

[1] Department of Physics, Riphah International University, Islamabad 44000, Pakistan; nasir.mehboob@riphah.edu.pk (N.M.); nabeelahmedkayani1234@gmail.com (N.A.); kashifahmed3322@gmail.com (K.A.); kasadiiui@gmail.com (A.A.); khalidbashir1969@gmail.com (K.B.)

[2] Faculty of Materials Science, Beijing University of Technology, Beijing 100124, China; mushtaqphy009@yahoo.com

[3] Department of Chemistry, College of Science, Taif University, P.O. Box 11099, Taif 21944, Saudi Arabia; k.althubeiti@tu.edu.sa

[4] Department of Physics, Government Post Graduate College, Nowshera 24100, Pakistan

[5] Department of Chemistry, University of Science and Technology China, Hefei 230026, China; fsultana@mail.ustc.edu.cn

[*] Correspondence: danyalahmad1938@gmail.com (D.A.); zaman.abid87@gmail.com (A.Z.)

Abstract: Cerium (Ce)-doped $Ni_{0.5}Cd_{0.5}Ce_xFe_{2-x}O_4$ ($0.0 \leq x \leq 0.20$) was synthesized using the sol–gel auto-combustion method. X-ray diffraction (XRD) analysis revealed that all the samples retained spinel cubic crystal structure with space group Fd3m at 800 °C. Crystal structure parameters, such as lattice constant, average crystallite size, and X-ray density were estimated from the major XRD (311) peak. Bulk density and porosity were also calculated. The average crystallite size was estimated to be in the range of 20–24 nm. SEM images displayed agglomerated particles with a porous morphology. The dielectric constant (ε') increased and the dielectric loss tangent (tanδ) decreased with rising Ce concentration. The hysteresis loop (M–H loop) was measured at room temperature using a vibrating-sample magnetometer (VSM), which showed a nonlinear decrease in magnetization and coercivity with increasing Ce concentration.

1. Introduction

Nanocrystalline ferrites have gained popularity in the field of electronic technology due to their outstanding feature of "ferrimagnetism" [1]. A cubic structure having the standard formula AB_2O_4 is commonly known as a "spinel" (where A signifies divalent cation and B stands for trivalent cation) [2]. As a result, spinel ferrites can be characterized as tightly packed cubic structures containing iron (Fe^{3+}) as a trivalent cation, yielding the structural formula AFe_2O_4. Most of the transition elements, such as Fe, Co, Ni, Zn, and Cd, as well as their composites, are examples of divalent cations (A). The structure of these ferrites is comparable to that of the naturally occurring mineral $MgAl_2O_4$ known as spinel. These ferrites are semiconducting in nature and are also known as ferrospinels or cubic ferrites [3,4]. Spinel ferrites have drawn much attention among researchers owing to their incredibly remarkable magnetic and electrical properties, such as high saturation magnetization, large magnetocrystalline anisotropy, high squareness ratio, low coercivity [5], high electric resistivity [6], high permeability [7], low eddy current losses [8], high Curie temperature, and mechanical hardness [9]. Spinel ferrites are extensively used in the fabrication of microwave absorbers owing to their high magnetic losses and huge resistivities [10]. These ferrites are also used in the frequency range of 3–30 GHz [2]. These materials are useful in metallurgical and other high-temperature sectors because they

have excellent thermodynamic stability, good electrical conductivity, and high corrosion resistance [11,12]. Spinel ferrites, with the general formula MFe_2O_4 (M = Ni, Zn, Mn, Co, Mg, etc.), are the most substantial, magnetic materials [13]. Ferrites have a spinel structure that belongs to the Fd3m space group. A cubic close-packed structure has 56 atoms, with 32 oxygen anions and 24 cations occupying 8 of the 64 tetrahedral sites (A sites) and 16 of the 32 octahedral sites (B sites), respectively [14]. There are two types of spinel ferrites that can be generally categorized [2].

(a) Normal Spinels: The general formula of normal spinels is $Me^{2+}[Fe_2^{3+}]O_4$. In normal spinels, tetrahedral or A-sites are involved with divalent ions (Me^{2+} cations) while trivalent ions are available at octahedral or B sites (Fe^{3+} cations).

(b) Inverse Spinels: The general formula of inverse spinels is $(Fe^{3+})[Me^{2+}Fe^{3+}]O_4$. In inverse spinels, divalent metal ions are present at the B-site, while trivalent metal ions are available either at the B site or at the A site [15].

Nickel spinel ferrites are spinel ferrites with a divalent cation of nickel. Nickel ferrite has a resistivity of more than 109 Ωm and is a high-resistance material [16]. Nickel ferrite has an inverted spinel structure. Fe^{3+} ions occupy 8 tetrahedral voids (A-sites), while Fe^{3+} and Ni^{2+} ions occupy 16 octahedral voids (B-sites) in equal proportion. Pristine nickel ferrites ($NiFe_2O_4$) have a degree of inversion of one. Because of their strong electric resistivity, reduced coercive field, slight saturation magnetization, and minimal hysteresis losses, nickel ferrites are characterized as soft ferrites [17,18]. Other advantageous qualities of such soft magnetic materials include excellent permeability at high frequencies, mechanical hardness, electrical properties, affordability, and minimal dielectric and eddy current losses [3,19].

These nanoparticles' magnetic conduct is primarily determined by their shape, purity, and magnetic stability, and they should maintain a single domain, appropriate coercivity, pure phase, mild magnetization, and the stable blocking properties that are most acceptable for their applications [20]. It is well known that smaller particles have higher remanent magnetization. As a result, smaller particles tend to have a single magnetic domain, whereas larger particles have several domains [21,22]. Ionic radii, particle size, and the existence and type of the substituent in the crystal lattice are all elements that influence the electrical and magnetic properties of ferrites [23].

Rare earth ion substitution into the spinel structure has become rare and interesting due to its dominance in many applications when compared with certain other substituted ferrite systems [24]. Rare earth ion replacement was reported to cause structural distortion as well as significant changes in electrical and magnetic characteristics [25,26]. This is because rare earth (RE) ions have unpaired 4f electrons and significant spin–orbit angular momentum coupling. The Fe–Fe interactions alter the electrical and magnetic characteristics of ferrites (spin coupling of the 3d electrons). When rare earth (RE) ions are incorporated into the spinel lattice, an RE–Fe interaction (3d–4f coupling) occurs, which improves the electrical and magnetic properties of the ferrites. Magnetocrystalline anisotropy in spinel ferrites is also determined by this feature. RE ions are increasingly used to improve the electromagnetic characteristics of spinel ferrites [27–31]. As a result, many researchers have been interested in studying the exceptional magnetic, optical, and electrical capabilities of RE-doped spinel ferrites. Rare earth lanthanides have high resistance and are good electrical insulators. They are commonly utilized to alter ferrites' structural, magnetic, and electrical properties. Their substitution was shown to produce high DC resistivity, low electrical permittivity, and low dielectric loss [32]. Many studies have looked at the effects of Fe^{3+} ion replacement with RE ions, such as La, Sm, Gd, Dy, Yb, Er, Tb, Ce, and Y [33]. As a result, the Ce ion was utilized as a dopant to better understand the processes of RE-doped ferrite. The Ce ion is known to offer substantial hybridization of the 4f states with 3d bands due to the existence of a larger 4f band. The improvement of electromagnetic characteristics of Li ferrite after Ce doping [34] and the enhancement of saturation magnetization with a decrease in coercivity in Ce doping Mn–Zn ferrite [35] are both interesting topics. Many methodologies are used for the synthesis of nanoparticles, either by an electrochemical

method, an electrodeposition method [36], or a cathodic electrodeposition method (CED), etc. [37].

The purpose of this study was to investigate the effects of the substitution of Ce^{3+} with Fe^{3+} in the amounts of 0, 4, 8, 12, 16, and 20 mol.%, according to the stoichiometry of $Ni_{0.5}Cd_{0.5}Ce_xFe_{2-x}O_4$ nano ferrites. The syntheses were carried out using the auto-combustion method. The samples were characterized in terms of structure, crystallite morphology, dielectric, and magnetic properties.

2. Material Synthesis and Characterizations

Samples with the chemical composition $Ni_{0.5}Cd_{0.5}Ce_xFe_{2-x}O_4$ ($0.0 \leq x \leq 0.20$) nano ferrites were prepared via the sol–gel auto-combustion method. Analytical grades $Ni(NO_3)_2 \cdot 6H_2O$, $Cd(NO_3)_2 \cdot 4H_2O$, $Ce(NO_3)_3 \cdot 6H_2O$, and $Fe(NO_3)_3 \cdot 9H_2O$ were used as precursors. According to stoichiometric calculation, 0.5 M solution of each $Ni(NO_3)_2 \cdot 6H_2O$, $Cd(NO_3)_2 \cdot 4H_2O$, and 2 M solution of $Ce(NO_3)_3 \cdot 6H_2O$, $Fe(NO_3)_3 \cdot 9H_2O$ were separately prepared in 100 mL of deionized water, and then all the solutions were mixed using citric acid as a chelating agent to acquire a homogenous solution with continuous stirring for 30 min. At that point, the solution was placed on a hot plate at 80 °C, maintaining the pH value at 7–8 by adding an ammonia solution, followed by constant stirring. After 5–6 h, the solution changed into a viscous brown gel, and afterward, a self-combustion occurred and the gel turned into ash. After completely crushing and grinding the ash, the fine powder was obtained and sintered at 800 °C in a furnace for 4 h.

The synthesized $Ni_{0.5}Cd_{0.5}Ce_xFe_{2-x}O_4$ (here, X = 0, 0.04, 0.08, 0.12, 0.16, 0.20) nano ferrites were characterized by an X-ray diffractometer (JDX-3532, JEOL, Tokyo, Japan), a scanning electron microscope (SEM), and an energy-dispersive X-ray spectroscopy (EDX) (JSM-5910, JEOL, Tokyo, Japan). All the samples were pressed into pellets of 12 mm diameter and 2.5–3 mm thickness by means of hydraulic press under the pressure of 30 MPa to study the dielectric behavior. Sodium silicate was utilized as a binder to obtain pellets and then sintered at 720 °C for 2 h. The dielectric constant (ε') and dielectric loss tangent (tan δ) were measured by using an LCR meter (Wayne Kerr version 6500B, Wayne Kerr Electronics, Bognor Regis, UK) at room temperature in the frequency range of a 100 Hz to 5 MHz BH-loop by a vibrating-sample magnetometer (VSM, Micro Sense, Hamm, Germany).

3. Results and Discussion

3.1. Structural Analysis

The X-ray diffraction (XRD) profile of the powdered $Ni_{0.5}Cd_{0.5}Ce_xFe_{2-x}O_4$ ($0.0 \leq x \leq 0.20$) samples sintered at 800 °C for 4 h is shown in Figure 1. XRD analysis identified the formation of the single-phase nanostructure, with no secondary phase revealed [38]. Thus, a series with complete incorporation of Ce into Ni-Cd ferrite samples was formed. The reflection peaks (2 2 0), (3 1 1), (2 2 2), (4 0 0), (4 2 2), (5 1 1), and (4 4 0) were identified according to JCPDS (Card No. 96-900-9926) and using Match! Software, having a spinel structure with an Fd3m space group. XRD evaluation proved that the substitution of rare earth Ce^{3+} ion up to 0.2 in nanoparticles did not alter the crystal structure and no second phase appeared.

Lattice parameter (*a*) was calculated for cubic structure by using formula (*1*) and average crystallite size (*D*) by the Debye–Scherrer formula [39];

$$a = d\sqrt{h^2 + k^2 + l^2} \tag{1}$$

$$D = \frac{k\lambda}{\beta \cos} \tag{2}$$

In Equations (1) and (2), *h*, *k*, and *l* are Miller indices and *d* is the interplanar distance (determined by Bragg's equation) and the full width half maxima (FWHM) of the major XRD peak.
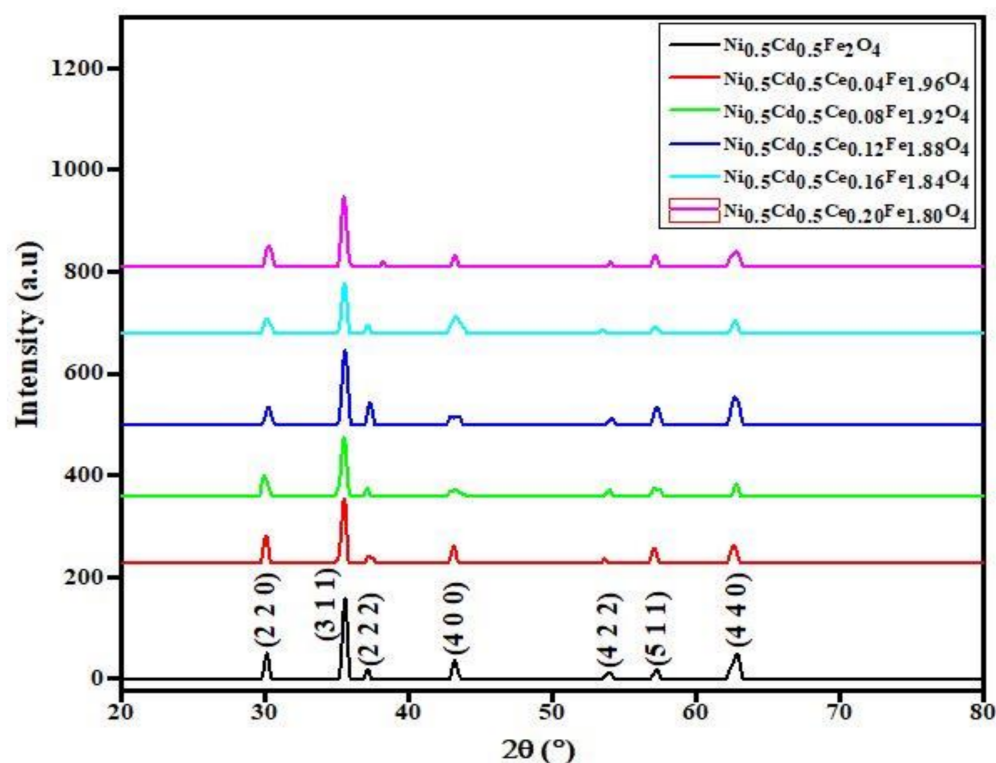
Figure 1. XRD patterns of $Ni_{0.5}Cd_{0.5}Ce_xFe_{2-x}O_4$ ($0.0 \leq x \leq 0.20$).

X-ray density and mass density. X-ray density is calculated by Equation (3).

$$d_X = \frac{8M}{N_a V} \tag{3}$$

where M is the molecular mass of the sample, V is the volume of the unit cell, and N_a is Avogadro's number (6.02×10^{23}). Molecular mass is multiplied by 8 because each primitive cell of spinel is made up of eight molecules.

The mass density of each sample was found by compacting the powders under 5000 psi pressure into pellets of a specific radius and thickness in a hydraulic press.

$$d_m = \frac{m}{\pi r^2 t} \tag{4}$$

here, m stands for mass (grams), t for thickness, and r = 6 mm for the radius of the pallet.

The formula for calculating porosity (P) is

$$P = \frac{d_x - d_m}{d_x} \times 100 \tag{5}$$

where d_x is X-ray density and d_m is mass density [40].

The lattice parameters, average crystallite sizes, X-ray density, mass density, and porosity are given in Table 1.

It can be seen in Figure 1 that the reflection planes shifted toward lower angles, unlike those investigated on doping Pr, Nd, Eu, and Gd in manganese zinc ferrite [41]. The inclusion of bigger ionic radii of Ce^{3+} (1.143 Å) in the lattice site of smaller ionic radii of Fe^{3+} (0.645 Å) may lead to lattice distortion, hence stresses shift the XRD peaks toward lower angles. The lattice parameters are not significantly affected by doping the Ce^{3+} ion in $Ni_{0.5}Cd_{0.5}Ce_xFe_{2-x}O_4$ ($0.0 \leq x \leq 0.20$). The average crystallite size is estimated in the range of 20–24 nm and shows nonlinear behavior with increasing dopant concentration. X-ray density was found to increase linearly. However, the bulk density shows nonlinear behavior with increasing Ce^{3+} concentration. The increase in X-ray density is due to the replacement of a larger molar mass of Ce ions. Bulk density depends on voids and

pores created during sintering, and porosity depends on the agglomeration and size of the particles. The porosity was increased by replacing Fe^{3+} ions with Ce^{3+} ions.

Table 1. XRD parameters of prepared samples.

Samples	Lattice Parameter(a) $(Å)^3$	Crystallite Size (D) (nm)	Volume $(Å)^3$	X-ray Density (g/cm^3)	Mass Density (g/cm^3)	Porosity (P) (%)
$Ni_{0.5}Cd_{0.5}Fe_2O_4$	8.372	21.76	586.86	5.916	3.304	31
$Ni_{0.5}Cd_{0.5}Ce_{0.04}Fe_{1.96}O_4$	8.385	23.99	589.74	5.962	3.381	43
$Ni_{0.5}Cd_{0.5}Ce_{0.08}Fe_{1.92}O_4$	8.385	21.76	589.74	6.038	3.134	47
$Ni_{0.5}Cd_{0.5}Ce_{0.12}Fe_{1.88}O_4$	8.372	20.33	586.85	6.144	3.647	41
$Ni_{0.5}Cd_{0.5}Ce_{0.16}Fe_{1.84}O_4$	8.381	22.92	588.77	6.201	3.051	49
$Ni_{0.5}Cd_{0.5}Ce_{0.20}Fe_{1.80}O_4$	8.385	21.84	589.74	6.266	3.279	47

3.2. Morphological Studies and Elemental Composition

The images of the surface morphology of $Ni_{0.5}Cd_{0.5}Fe_2O_4$ and Ce-doped $Ni_{0.5}Cd_{0.5}Fe_2O_4$ annealed at 800 °C are shown in Figure 2. The scan part of the samples shows the agglomeration of particles with sponge morphology. However, above x = 0.04, the morphology was little changed, and the particles appeared to be pores of about 2–4 μm in size (Table 2). From SEM micrographs, it appears that the average grain size of nanoparticles in the range from 23 to 25 μm was calculated by using ImageJ software.
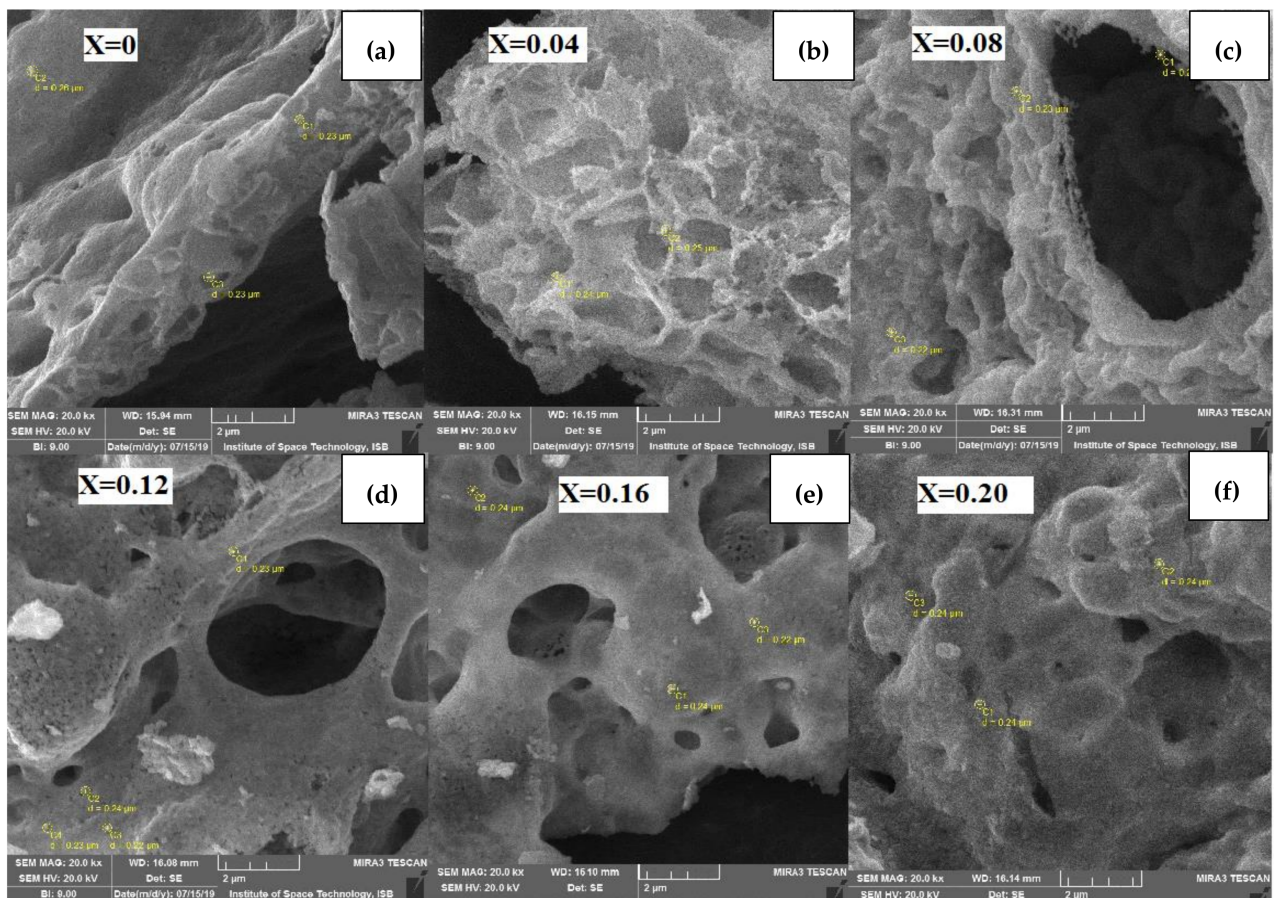

Figure 2. SEM images of samples $Ni_{0.5}Cd_{0.5}Ce_xFe_{2-x}O_4$ (0.0 ≤ x ≤ 0.20), (**a**) X = 0; (**b**) X = 0.04; (**c**) X = 0.08; (**d**) X = 0.12; (**e**) X = 0.16 and (**f**) X = 0.20.

Table 2. Particle sizes obtained from SEM analysis for cerium doped in $Ni_{0.5}Cd_{0.5}Fe_2O_4$ nanoparticles.

Sample Name	Particles Size (µm)	Deviation in Particle Size (nm)
$Ni_{0.5}Cd_{0.5}Fe_2O_4$	0.24	1.489
$Ni_{0.5}Cd_{0.5}Ce_{0.04}Fe_{1.96}O_4$	0.25	5.962
$Ni_{0.5}Cd_{0.5}Ce_{0.08}Fe_{1.92}O_4$	0.23	2.983
$Ni_{0.5}Cd_{0.5}Ce_{0.12}Fe_{1.88}O_4$	0.23	2.983
$Ni_{0.5}Cd_{0.5}Ce_{0.16}Fe_{1.84}O_4$	0.23	2.983
$Ni_{0.5}Cd_{0.5}Ce_{0.20}Fe_{1.80}O_4$	0.24	1.489

The EDX pattern shown in Figure 3 confirms the presence of constituent elements in all samples with no impurity peaks. Table 3 shows that the estimated composition of Ce^{3+}-doped $Ni_{0.5}Cd_{0.5}Fe_2O_4$ nanoparticles is almost stoichiometric. The EDX pattern confirms the homogeneous mixing of Ce^{3+} among Ni, Cd, Fe, and O in pure and doped samples. No impurity peaks were found in the EDX spectra for characterization of the purity of organized samples, as shown in Figure 3.
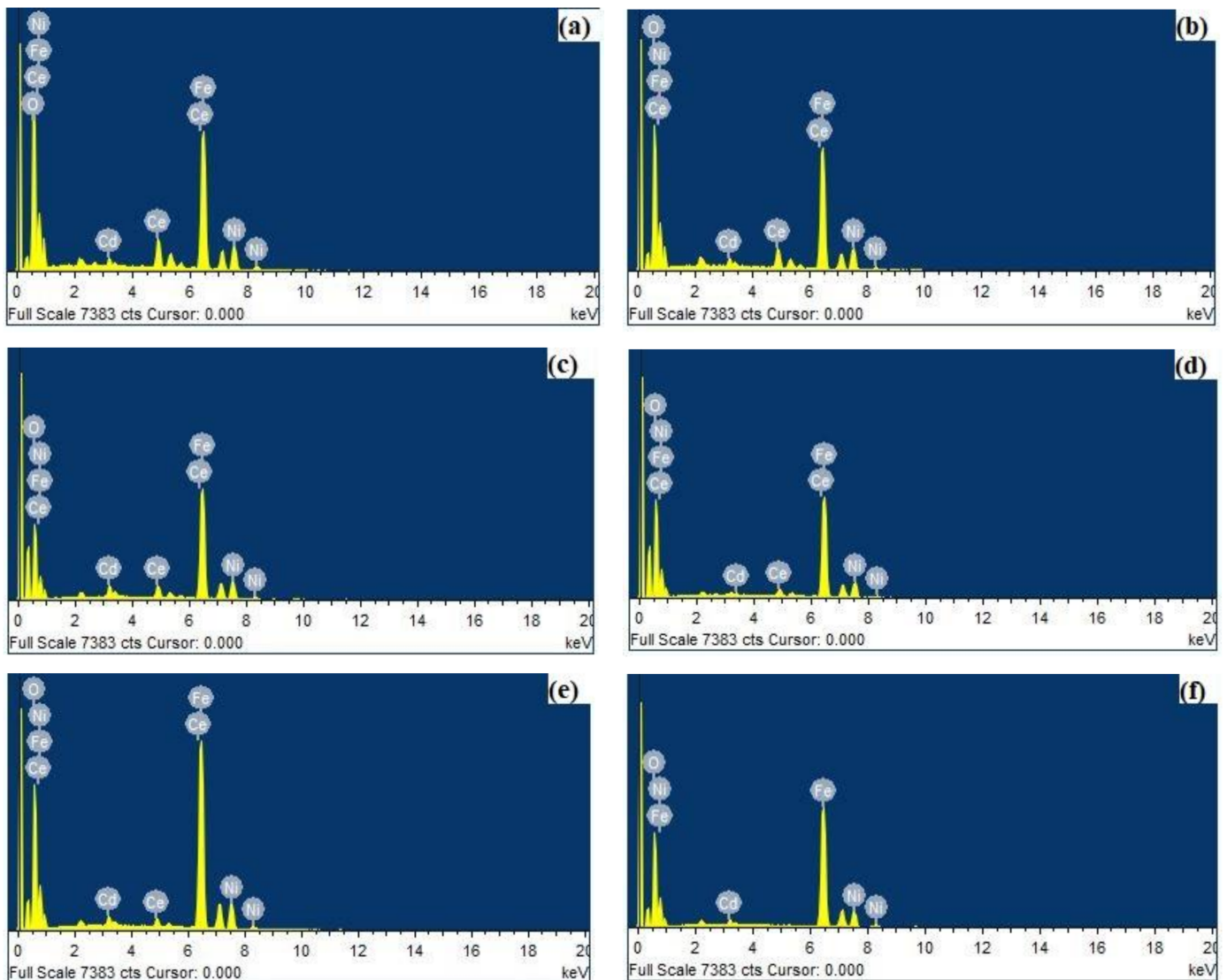

Figure 3. EDX micrographs for prepared nanoparticles (**a**) $Ni_{0.5}Cd_{0.5}Fe_2O_4$, (**b**) $Ni_{0.5}Cd_{0.5}Ce_{0.04}Fe_{1.96}O_4$, (**c**) $Ni_{0.5}Cd_{0.5}Ce_{0.08}Fe_{1.92}O_4$, (**d**) $Ni_{0.5}Cd_{0.5}Ce_{0.12}Fe_{1.88}O_4$, (**e**) $Ni_{0.5}Cd_{0.5}Ce_{0.16}Fe_{1.84}O_4$, and (**f**) $Ni_{0.5}Cd_{0.5}Ce_{0.20}Fe_{1.80}O_4$.

Table 3. Atomic percentage composition from EDX in $Ni_{0.5}Cd_{0.5}Ce_xFe_{2-x}O_4$ ($0.0 \leq x \leq 0.20$) nanoparticles.

Elements (At %)	$Ni_{0.5}Cd_{0.5}Ce_xFe_{2-x}O_4$					
	X = 0	**X = 0.04**	**X = 0.08**	**X = 0.12**	**X = 0.16**	**X = 0.20**
O	24.89	23.69	27.12	21.71	28.52	28.42
Fe	60.84	57.66	53.59	52.71	45.13	44.01
Ni	12.34	12.61	12.71	12.77	12.61	11.47
Cd	1.93	2.30	1.48	4.69	2.67	1.95
Ce	-	3.74	5.10	8.13	11.08	14.14

3.3. Dielectric Properties

Frequency dependent dielectric properties were measured by using an LCR meter. By measuring parallel equivalent capacitance (C_p), different parameters, such as dielectric constant (ε') and dielectric loss ($\tan \delta$), were calculated by the following expressions [42].

$$\varepsilon' = \frac{C_p d}{\varepsilon_o A}$$

$$\tan \delta = \frac{\varepsilon''}{\varepsilon'}$$

where d is the thickness of a pellet, A is the surface area of the sample, and ε_o is the permittivity of free space.

Figure 4 shows the dielectric constant (ε') versus log of frequency (f) of all the samples measured at room temperature. As seen in Figure 4, Ce-doped $Ni_{0.5}Cd_{0.5}Fe_2O_4$ ferrite nanoparticles show a high dielectric constant at low frequency (100 Hz), the value of which then sharply decreases and becomes independent at high frequency. This is the common trend in ferrites' nanoparticles. However, at medium frequency (400 Hz to 8 KHz), the dielectric constant decreases with a weak slope. The frequency-dependent dielectric behavior can be explained based on Koops' [43] theory by considering two layers of the Maxwell–Wagner model [44]. According to this phenomenological theory, inhomogeneous ferrite nanoparticles consist of highly conducting grains with respect to the grain boundaries that separate them. When the electric field is applied, the charges localize at the grain boundaries due to poor conducting grain boundaries having different relaxation times $\frac{\varepsilon'}{\sigma}$, which causes interfacial polarization. The high dielectric constant at low frequency is due to the polarization and hopping conduction processes in nanoparticles following the changing electric field, as a result of which the dipole moments are well aligned. As the frequency of the electric field increases, the dielectric constant decreases and becomes constant at higher frequency regions. Due to the rapid oscillating field, the alignment of the dipole moments is distorted and, therefore, the dipoles lag behind the applied field [45,46].

Figure 5 shows that at low frequency, the tangent loss is minimum and the dielectric constant is maximum, meaning that the nanoparticles are polarized. At medium frequency, the polarization decreases, so the tangent loss increases and becomes maximum. With further increase in frequency, the tangent loss decreases sharply and becomes independent of frequency.
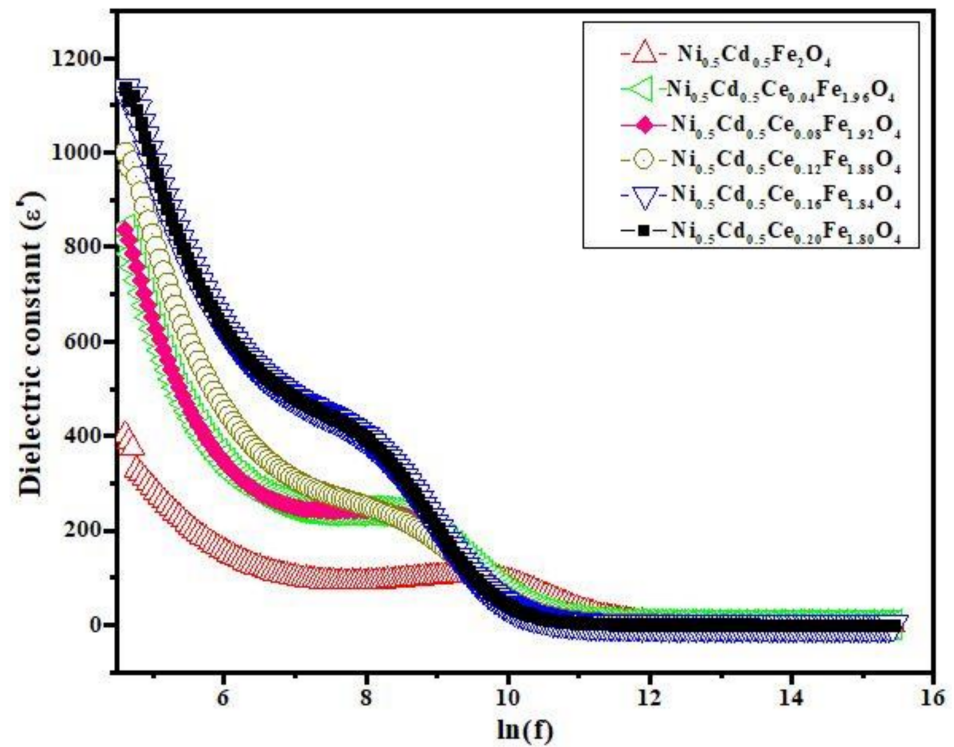
Figure 4. Dielectric constant vs. ln(f) plot for $Ni_{0.5}Cd_{0.5}Ce_xFe_{2-x}O_4$ ($0.0 \leq x \leq 0.20$).
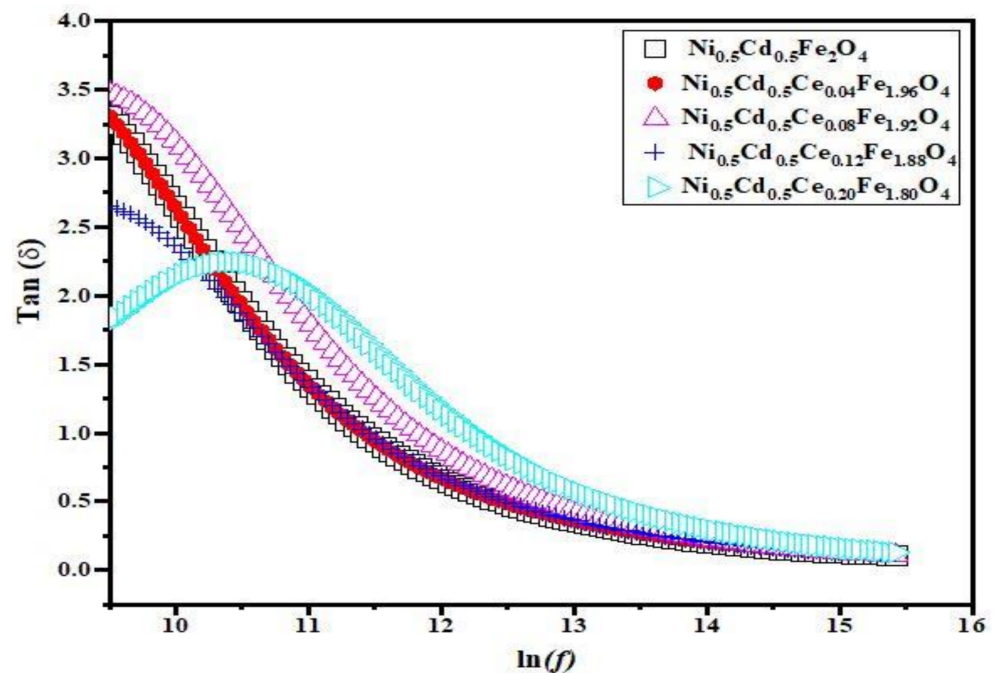
Figure 5. Tangent loss (tan δ) vs. ln(f) plot for $Ni_{0.5}Cd_{0.5}Ce_xFe_{2-x}O_4$ ($0.0 \leq x \leq 0.20$).

3.4. Magnetic Properties

The magnetic properties of Ce^{3+}-doped nanoparticles of $Ni_{0.5}Cd_{0.5}Ce_xFe_{2-x}O_4$ powdered samples were investigated by a vibrating-sample magnetometer (VSM). The measured hysteresis loops at room temperature are shown in Figure 6. Saturation magnetization (M_s), coercivity (H_c), remanent magnetization (M_r), and remanence ratio were extracted from M–H curves and shown in Table 4. The grain size, magnetic nature of cation substitu-

tion, A–B exchange interaction, and magnetocrystalline anisotropy all affect the magnetic characteristics of ferrites.
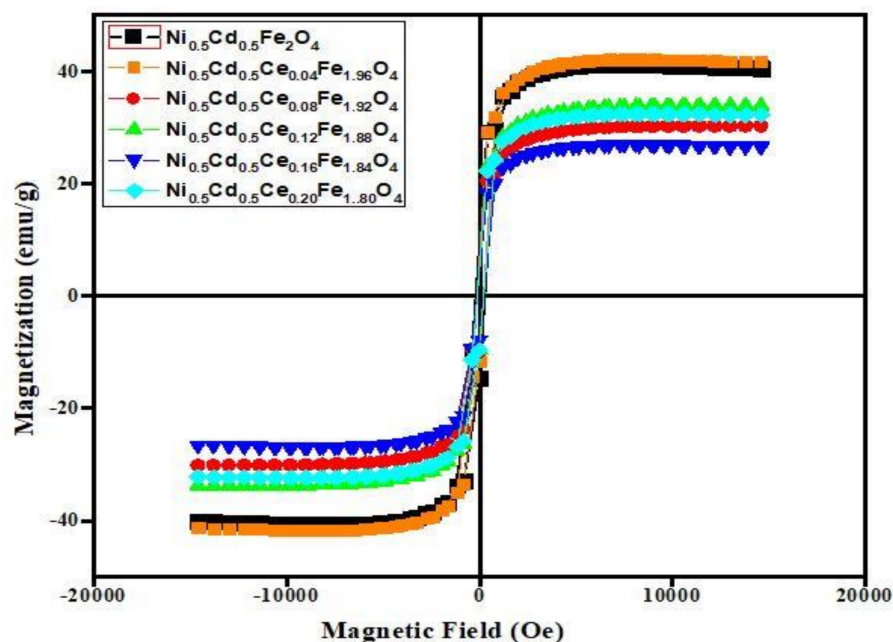

Figure 6. Magnetization vs. magnetic field graph for $Ni_{0.5}Cd_{0.5}Ce_xFe_{2-x}O_4$ ($0.0 \leq x \leq 0.20$).

Table 4. Different values of H_c, M_r, M_s and ratios of M_r/M_s for $Ni_{0.5}Cd_{0.5}Ce_xFe_{2-x}O_4$ ($0.0 \leq x \leq 0.20$) nanoparticles.

Composition	Saturation Magnetization M_s (emu/g)	Remanent Magnetization M_r (emu/g)	Coercivity H_c (Oe)	Remanence Ratio M_r/M_s
$Ni_{0.5}Cd_{0.5}Fe_2O_4$	40.7	11.8	227	0.29
$Ni_{0.5}Cd_{0.5}Ce_{0.04}Fe_{1.96}O_4$	41.3	9.3	174	0.23
$Ni_{0.5}Cd_{0.5}Ce_{0.08}Fe_{1.92}O_4$	30.5	7.3	185	0.24
$Ni_{0.5}Cd_{0.5}Ce_{0.12}Fe_{1.88}O_4$	33.7	7.6	178	0.23
$Ni_{0.5}Cd_{0.5}Ce_{0.16}Fe_{1.84}O_4$	26.5	5.8	170	0.22
$Ni_{0.5}Cd_{0.5}Ce_{0.20}Fe_{1.80}O_4$	32.2	6.8	164	0.21

It can be seen from Figure 6 and the values in Table 4 that the saturation magnetization (M_s), coercivity (H_c), and remanence (M_r) nonlinearly decreased with the increase of Ce^{3+} concentration in $Ni_{0.5}Cd_{0.5}Ce_xFe_{2-x}O_4$. The decreasing M_s is due to the replacement of Fe^{3+} ions at the B-site with paramagnetic Ce^{3+} ions possessing a smaller magnetic moment. In addition, Ce^{3+} at the B-site reduces A–B exchange interactions [47]. The nonlinearity in M_s can be related to grain size, magnetocrystalline anisotropy, and A–B super exchange interaction. Coercivity in the multidomain regime is shown to be inversely proportional to particle size [47].

Ce ions clearly replace Fe ions in the octahedral position, based on cation distribution. The magnetic moment (μB) of paramagnetic Ce^{3+} is 2.2 BM, and the magnetic moment (μB) of the Fe^{3+} ion is 5 BM in the current ferrite system under examination. Doping nickel ferrites with Ce should raise the saturation magnetization value, according to their magnetic moments, but the obtained values show that the saturation magnetization value has decreased with increasing dopant concentration [48].

4. Conclusions

Cerium-doped nickel ferrite nanoparticles with the general formula $Ni_{0.5}Cd_{0.5}Ce_xFe_{2-x}O_4$ ($0.0 \leq x \leq 0.20$) have been successfully synthesized by the sol–gel auto-combustion method. Samples were characterized by XRD, SEM, EDX, an LCR meter, and VSM. XRD confirmed the spinel cubic crystal structure, and the crystallite size of all six prepared nanoparticles was calculated through Scherrer's equation, which showed the crystallite size changes randomly with an increase in cerium concentration. SEM analysis determined that the shape of nanoparticles was irregular, and the range of particle size was from 23 μm to 25 μm. EDX evaluation showed the purity of the samples. The dielectric constant and tangent loss were studied in a frequency range of 100 Hz to 6 MHz. The dielectric parameters of all the samples were explained on the basis of charge polarization. The dielectric constant was highly increased and the loss tangent decreased with doped concentration. The saturation magnetization and coercivity decreased with the substitution of cerium Ce^{3+} ions, which demonstrates that it is a soft magnetic material with low saturation.

Author Contributions: Conceptualization, K.A (Kashif Ahmed). and F.S.; Formal analysis, K.A. (Kashif Ahmed) and A.A.; Funding acquisition and Project administration, K.A.(Khaled Althubeiti); Resources, N.A.; Data curation, N.A. and K.B.; Methodology and Supervision, N.M.; Vali-dation, M.M. and K.B.; Visualization, F.S., M.M. and A.A.; Writing—original draft, D.A.; Writing—review & editing and Software, A.Z. All authors have read and agreed to the published version of the manuscript.

Institutional Review Board Statement: Not applicable.

Informed Consent Statement: Not applicable.

Data Availability Statement: Not applicable.

Conflicts of Interest: There is no conflict of interest.

References

1. Sabri, N.G. The outermembrane proteins profile of *Salmonella enterica* serotypes Enteritidis, Muenster, Florian, Omuna and Noya and their dendrogram analysis. *Int. J. Adv. Res.* **2013**, *2*, 182–187.
2. Atiq, S.; Majeed, M.; Ahmad, A.; Abbaas, S.K.; Saleem, M.; Riaz, S.; Naseem, S. Synthesis and investigation of structural, morphological, magnetic, dielectric and impedance spectroscopic characteristics of Ni-Zn ferrite nanoparticles. *Ceram. Int.* **2017**, *43*, 2486–2494. [CrossRef]
3. Ditta, A.; Khan, M.A.; Junaid, M.; Khalil, R.M.A.; Warsi, M.F. Structural, magnetic and spectral properties of Gd and Dy co-doped dielectrically modified Co-Ni ($Ni_{0.4}Co_{0.6}Fe_2O_4$) ferrites. *Physica B* **2017**, *507*, 27–34. [CrossRef]
4. Jalaiah, K.; Babu, K.V. Structural, magnetic and electrical properties of nickel doped Mn-Zn spinel ferrite synthesized by sol-gel method. *J. Magn. Magn. Mater.* **2017**, *423*, 275–280. [CrossRef]
5. Heiba, Z.K.; Mohamed, M.B.; Hamdeh, H.H.; Ahmed, M.A. Structural analysis and cations distribution of nanocrystalline $Ni_{1-x}Zn_xFe_{1.7}Ga_{0.3}O_4$. *J. Alloys Compd.* **2015**, *618*, 755–760. [CrossRef]
6. Liu, Q.; Lv, L.; Zhou, J.P.; Chen, X.M.; Bian, X.B.; Lu, P.J. Influence of nickel-zinc ratio on microstructure, magnetic and dielectric properties of $Ni_{1-x}Zn_xFe_2O_4$ ferrites. *Ceram. Proc. Res.* **2012**, *13*, 110–116.
7. Mukharjee, S.; Pradip, S.; Mishra, A.K.; Das, D. Zn substituted $NiFe_2O_4$ with very high saturation magnetization and negligible dielectric loss synthesized via a soft chemical route. *Appl. Phys. A* **2014**, *114*, 389–393. [CrossRef]
8. Ghasemi, A.; Mousavinia, M. Structural and magnetic evaluation of substituted $NiZnFe_2O_4$ particles synthesized by conventional sol–gel method. *Ceram. Int.* **2014**, *40*, 2825–2834. [CrossRef]
9. Wu, X.; Chen, W.; Wu, W.; Li, H.; Lin, C. Structural and Magnetic Properties Evolution of Li-Substituted $Co_{0.5}Ni_{0.5}Fe_2O_4$ Ferrite. *J. Electron. Mater.* **2017**, *46*, 199–207. [CrossRef]
10. Xie, J.L.; Han, M.; Chen, L.; Kuang, R.; Deng, L.J. Microwave-absorbing properties of NiCoZn spinel ferrites. *Magn. Magn. Mater.* **2007**, *314*, 37–42. [CrossRef]
11. Olsen, E.; Thonstad, J. Nickel ferrite as inert anodes in aluminium electrolysis: Part I Material fabrication and preliminary testing. *J. Appl. Electrochem.* **1999**, *29*, 293–299. [CrossRef]

12. Berchmans, L.J.; Selvan, R.K.; Augustin, C.O. Evaluation of Mg^{2+}-substituted $NiFe_2O_4$ as a green anode material. *Mater. Lett.* **2004**, *58*, 1928–1933. [CrossRef]

13. Sugimoto, M. The past, present, and future of ferrites. *J. Am. Ceram. Soc.* **1999**, *82*, 269–279. [CrossRef]

14. Verwey, J.W.; Heilmann, E.L. Physical properties and cation arrangement of oxides with spinel structures II. Electronic conductivity. *J. Chem. Phys.* **1947**, *15*, 181–187. [CrossRef]

15. Valenzuela, R. *Magnetic Ceramics*; Cambridge University Press: Cambridge, UK, 2005; Volume 4.

16. Smit, J.; Wijn, H.P.J. *Ferrites, Philips Technical Library*; Springer: Eindhoven, The Netherlands, 1959.

17. Ishaque, M.; Islam, M.U.; Khan, M.A.; Rahman, I.Z.; Genson, A.; Hampshire, S. Structural, electrical and dielectric properties of yttrium substituted nickel ferrites. *Phys. B Phys. Condens. Matter* **2010**, *405*, 1532–1540. [CrossRef]

18. Grigorova, M.; Blythe, H.J.; Blaskov, V.; Rusaniv, V.; Petkov, V.; Masheva, V.; Nitianova, D.; Martinez, L.M.; Mŭnoz, J.S.; Mikhov, M. Magnetic properties and Mössbauer spectra of nanosized $CoFe_2O_4$ powders. *J. Magn. Magn. Mater.* **1998**, *183*, 163–172. [CrossRef]

19. Ishino, K.; Narumiya, Y. Development of magnetic ferrites: Control and application of losses. *Ceram. Soc. Bull.* **1987**, *66*, 1469–1474.

20. Maaz, K.; Khalid, W.; Mumtaz, A.; Hasanain, S.K.; Liu, J.; Duan, J.L. Magnetic characterization of $Co_{1-x}Ni_xFe_2O_4$ ($0 \leq x \leq 1$) nanoparticles prepared by co-precipitation route. *Phys. E Low-Dimens. Syst. Nanostruct.* **2009**, *41*, 593–599. [CrossRef]

21. Maensiri, S.; Masingboon, C.; Boonchomb, B.; Seraphin, S. A simple route to synthesize nickel ferrite ($NiFe_2O_4$) nanoparticles using egg white. *Scr. Mater.* **2007**, *56*, 797–800. [CrossRef]

22. Zhang, D.; Tong, Z.; Xu, G.; Li, S.; Ma, J. Templated fabrication of $NiFe_2O_4$ nanorods: Characterization, magnetic and electrochemical properties. *Solid State Sci.* **2009**, *11*, 113–117. [CrossRef]

23. Batoo, K.M.; Ansari, M.S. Low temperature-fired Ni-Cu-Zn ferrite nanoparticles through auto-combustion method for multilayer chip inductor applications. *Nanoscale Res. Lett.* **2012**, *7*, 112. [CrossRef]

24. Nikumbh, A.K.; Pawar, R.A.; Nighot, D.V.; Gugale, G.S.; Sangale, M.D.; Khanvilkar, M.B.; Nagawade, A.V. Structural, electrical, magnetic and dielectric properties of rare-earth substituted cobalt ferrites nanoparticles synthesized by the co-precipitation method. *J. Magn. Magn. Mater.* **2014**, *355*, 201–209. [CrossRef]

25. Sun, G.L.; Li, J.B.; Sun, J.J.; Yang, X.Z. The influences of Zn^{2+} and some rare-earth ions on the magnetic properties of nickel-zinc ferrites. *J. Magn. Magn. Mater.* **2004**, *281*, 173–177. [CrossRef]

26. Rezlescu, N.; Rezlescu, E.; Pasnicu, C.; Craus, M.L. Effects of the rare-earth ions on some properties of a nickel-zinc ferrite. *J. Phys. Condens. Matter* **1994**, *6*, 5707–5716. [CrossRef]

27. Hochschild, R.; Fuess, H. Rare-earth doping of nickel zinc ferrites. *J. Mater. Chem.* **2000**, *10*, 539–542. [CrossRef]

28. Kahn, M.L.; Zhang, Z. Synthesis and magnetic properties of $CoFe_2O_4$ spinel ferrite nanoparticles doped with lanthanide ions. *J. Appl. Phys. Lett.* **2001**, *78*, 3651–3653. [CrossRef]

29. Jiang, J.; Li, L.C.; Xu, F.; Xie, Y.L. Preparation and magnetic properties of Zn-Cu-Cr- Sm ferrite via a rheological phase reaction method. *Mater. Sci. Eng. B* **2007**, *137*, 166–169. [CrossRef]

30. Jiang, J.; Li, L.C.; Xu, F. Structural analysis and magnetic properties of Gd-doped Li-Ni ferrites prepared by the rheological phase method. *J. Rare Earths* **2007**, *25*, 79–83. [CrossRef]

31. Jiang, J.; Li, L.C.; Xu, F.; Li, Z.T. Structural and magnetic properties of La-doped Li- Ni ferrite. *J. Rare Earths* **2005**, *23*, 259–262.

32. Chand, J.; Singh, M. Electric and dielectric properties of $MgGd_{0.1}Fe_{1.9}O_4$ ferrite. *J. Alloys Compd.* **2009**, *486*, 376–379. [CrossRef]

33. Sattar, A.A.; El-Shokrofy, K.M. Rare earth doping effect on the electrical properties of Cu-Zn ferrites. *Le J. De Phys. IV* **1997**, *7*, C1-245–C1-246.

34. Verma, V.; Kotnala, R.K.; Pandey, V.; Kothari, P.C.; Radhapiyari, L.; Matheru, B.S. The effect on dielectric losses in lithium ferrite by cerium substitution. *J. Alloys Compd.* **2008**, *466*, 404–407. [CrossRef]

35. Xiang, J.; Shen, X.; Zhu, Y. Effects of Ce^{3+} doping on the structure and magnetic properties of Mn-Zn ferrite fibers. *Rare Met.* **2009**, *28*, 151–155. [CrossRef]

36. Jouyandeh, M.; Zarrintaj, P.; Ganjali, M.R.; Ali, J.A.; Karimzadeh, I.; Aghazadeh, M.; Ghaffari, M.; Saeb, M.R. Curing epoxy with electrochemically synthesized $Gd_xFe_{3-x}O_4$ magnetic nanoparticles. *Prog. Org. Coat.* **2019**, *136*, 105245. [CrossRef]

37. Jouyandeh, M.; Ali, J.A.; Aghazadeh, M.; Formela, K.; Saeb, M.R.; Ranjbar, Z.; Ganjali, M.R. Curing epoxy with electrochemically synthesized $Zn_xFe_{3-x}O_4$ magnetic nanoparticles. *Prog. Org. Coat.* **2019**, *136*, 105246. [CrossRef]

38. Sharifi, S.; Yazdani, A.; Rahimi, K. Incremental substitution of Ni with Mn in $NiFe_2O_4$ to largely enhance its supercapacitance properties. *Sci. Rep.* **2020**, *10*, 1–15. [CrossRef]

39. Zaman, A.; Uddin, S.; Mehboob, N.; Ali, A.; Ahmad, A.; Bashir, K. Effect of Zr^{4+} on the structural and microwave dielectric properties of $CaTiO_3$ ceramics. *Ferroelectrics* **2021**, *577*, 143–152. [CrossRef]

40. Zaman, A.; Uddin, S.; Mehboob, N.; Ali, A. Structural investigation and improvement of microwave dielectric properties in Ca$(Hf_xTi_{1-x})O_3$ ceramics. *Phys. Scr.* **2020**, *96*, 025701. [CrossRef]

41. Ansari, M.M.N.; Khan, S.; Ahmad, N. Effect of R^{3+} (R = Pr, Nd, Eu and Gd) substitution on the structural, electrical, magnetic, and optical properties of Mn-ferrite nanoparticles. *J. Magn. Magn. Mater.* **2018**, *465*, 81–87. [CrossRef]

42. Abbas, M.; Ullah, R.; Ullah, K.; Sultana, F.; Mahmood, A.; Mateen, A.; Zhang, Y.; Ali, A.; Althubeiti, K.; Mushtaq, M.; et al. Structural, optical, electrical and dielectric properties of $(Sr_{1-x}Mg_x)(Sn_{0.5}Ti_{0.5})O_3$ (X = 0.00, 0.25, 0.50, 0.75) ceramics via solid state route. *Ceram. Int.* **2021**, *47*, 30129–30136. [CrossRef]

43. Koops, C.G. On the dispersion of resistivity and dielectric constant of somesemiconductors at audio frequencies. *Phys. Rev.* **1951**, *83*, 121–124. [CrossRef]

44. Iwamoto, M. Maxwell–Wagner Effect. In *Encyclopedia of Nanotechnology*; Springer: Dordrecht, The Netherlands, 2015.

45. Dixit, G.; Singh, J.P.; Chen, C.L.; Dong, C.L.; Srivastava, R.C.; Agrawal, H.M.; Pong, W.F.; Asokan, K. Study of structural, morphological and electrical properties of Ce doped $NiFe_2O_4$ nanoparticles and their electronic structure investigation. *J. Alloys Compd.* **2013**, *581*, 178–185. [CrossRef]

46. Reetu; Agarwal, A.; Sanghi, S.; Ashima; Ahlawat, N.; Monica. Phase transformation, dielectric and magnetic properties of Nb doped $Bi_{0.8}Sr_{0.2}FeO_3$ multiferroics. *J. Appl. Phys.* **2012**, *111*, 113917. [CrossRef]

47. George, L.; Viji, C.; Mathew, H.; Mohammed, E.M. Structural, Dielectric, Magnetic and Optical Properties of Cerium Substituted Ni-Zn Mixed Ferrite. *Mater. Sci. Res. India* **2017**, *14*, 133–139. [CrossRef]

48. Hashim, M.; Raghasudha, M.; Meena, S.S.; Shah, J.; Shirsath, S.E.; Kumar, S.; Ravinder, D.; Bhatt, P.; Kumar, R.; Kotnala, R.K. Influence of rare earth ion doping (Ce and Dy) on electrical and magnetic properties of cobalt ferrites. *J. Magn. Magn. Mater.* **2018**, *449*, 319–327. [CrossRef]